Jordan Journal of Civil Engineering, Volume **17**, No. **2**, **2023**
DOI: https://doi.org/10.14525/JJCE.v17i2.14

Damage Mechanism on Different Joint Types of Plain Concrete under Uniaxial Compression

Shanshan Guo $^{1)*}$, ***Deyong Cui*** $^{2)}$ ***and Liang Lv*** $^{3)}$

$^{1)}$ Research Scholar, Engineering Institute, Zhengzhou Technology and Business University,
Zhengzhou, 451400 China. E-Mail: guo1054644468@163.com
*Corresponding Author. https://orcid.org/0009-0001-8507-0088
$^{2)}$ Senior Engineer, Henan Provincial Academy of Building Research Co., Ltd.,
Zhengzhou, 450053 China. E-Mail: 287920439@qq.com
$^{3)}$ Ph.D. Candidate, School of Civil Engineering, Southwest Jiaotong University,
Chengdu, 610031 China. E-Mail: 347843875@qq.com

ABSTRACT

Excavation of tunnels or chambers causes crack initiation, propagation and coalescence, resulting in the instability and destruction of underground projects. Understanding the damage mechanism of joint rock-like materials is important for maintaining the stability of concrete construction. Based on the Mohr–Coulomb criterion and Lemaitre strain equivalence hypothesis, the coupling-damage constitutive model of rock masses was improved for application to plain concrete. Parameters including the mesoscopic and macro-meso coupling damage variables, as well as the fractal dimension, were calculated to realize the non-linear mechanical behaviour during damage evolution. The rationality of the model was verified by comparing experimental and theoretical parameters. Results revealed that the coupled-damage constitutive model of rock masses has a good applicability to plain concrete. Furthermore, two main factors affected the damage deformation: the number of joints and the inclination angle. As the number of joints increased, the early damage accumulation increased and the inflection point of the damage rate occurred in advance. The damage deformation varied significantly when the inclination angle was changed. The cumulative damage curve of the plain-concrete specimens is shown as the evolution law of an *S*-type curve. Both peak strength and elastic modulus were positively correlated with the damage variable. Moreover, a smaller peak strength resulted in a larger fractal dimension and coupling-damage variable.

KEYWORDS: Rock mass, Joint inclination angle, Mesoscopic, Macroscopic, Fractal dimension, Coupling-damage constitutive model.

INTRODUCTION

Excavation of tunnels or chambers causes crack initiation, propagation and coalescence, resulting in the instability and destruction of underground projects (Lin et al., 2020). To a certain extent, the mechanical characteristics of engineering rock masses are affected by these defects (Liu et al., 2016a; Fan et al., 2018). Owing to the rapid developments in technology, common building materials are gradually being substituted with artificial rock masses (rock-like materials), including plain concrete, plaster and reinforced concrete, in the fields of construction and transportation (Yousuf et al., 2019). Therefore, it is important to ensure the safety and stability of structures by studying the influence of self-cracks on the mechanical characteristics of rock-like engineering materials (Qing et al., 2018).

Three common methods; namely, experimental research, theoretical derivations and numerical simulations, can reveal the damage mechanisms of rock masses under loading (Yang et al., 2019). In experimental studies, owing to the difficulties of the

---

Received on 8/7/2022.
Accepted for Publication on 7/2/2023.

prepared specimens, most researchers have often used indoor model tests to study fractural characteristics, including the joint inclination angle and number of joints. Hoek and Bieniawski (1965) investigated the damage mechanisms of single-joint rock masses at different joint angles. Results revealed that cracks spread more easily when the joint inclination angle is close to the failure angle under uniaxial compression. Bobet and Einstein (1998) investigated the damage laws of double-joint specimens under uniaxial compression. Crack expansion had a direct correlation with the joint inclination angle and rock-bridge length. Chen et al. (2011) and Zeng et al. (2019) conducted uniaxial-compression tests on intermittent and parallel multi-joint gypsum specimens. The joint inclination angle and connectivity had an evident effect on the mechanical parameters. Kawamoto et al. (1988) integrated the damage theory into the constitutive equation of a fractured rock mass based on the geometric damage theory. Zhou et al. (1998) simplified the fracture-propagation mechanism by considering the elastic and damage coupling of the rock mass. Subsequently, a damage-coupling constitutive model was constructed and the damage statistical strength theory was further improved (Cao et al., 2017). A macro-meso damage-coupling constitutive equation was established based on the Lemaitre equivalent-strain hypothesis and statistical theory (Zhang and Chen, 2017; Chen et al., 2018a; Chen and Qiao, 2018b). The equation showed that the initial damage of the pre-fabricated joints affected the rock-mass failure process. Consequently, the static and dynamic damage-evolution processes of jointed rock masses can be simulated (Guan and Chen, 2021; Zhang et al., 2015; Liu et al., 2016b). Additionally, fractal theory was used in quantitative calculations during the damage process. With the development of numerical simulations and improvements in constitutive theories, the dynamic damage process of rock masses has become increasingly intuitive. Thomas and Belytschko (2010) proposed a finite-element method for the minimum re-cogging of crack growth, which can approximately explain crack propagation.

The damage mechanism of rock masses is mainly focused on factors, such as type inclination angle, row distance and centre distance of cracks. However, limited research on the comparison of multiple joints of plain concrete exists. This study aimed to: (1) study the damage mechanism of rock-like materials using plain concrete as the research object, (2) verify the rationality of the model through a comparative analysis by introducing experimental data and (3) reveal the difference between the theoretical and experimental results by discussing the relationship between the fractal-box dimensions of the joint surface and the coupling-damage variable, peak strength and joint inclination angle. Considering the initial damage of the pre-fabricated joints, the macro-damage variable and joint-coupling influence coefficient were revised. Therefore, the macro-meso coupling-damage constitutive model of plain concrete was improved.

Statistical Damage Constitutive Construction under Uniaxial Compression

Statistical Constitutive Models of Rock Meso-damage

Under Lemaitre strain equivalence assumptions, the rock-mass damage constitutive model is defined by Eq. (1) (Lemaitre, 1984).

$$\sigma = E\varepsilon(1-D), \tag{1}$$

where σ denotes the nominal stress, E denotes the elastic modulus, ε denotes the strain and D denotes the damage variable under compression. Based on the Mohr–Coulomb criterion and Hooke’s law, meso-scopic rock failure is a continuous damage process. Weibull used the statistical probability theory to describe the heterogeneity of materials, explaining the relationship between material strength, deformation and failure. When the micro-element strength inside rock F obeys the Weibull probability distribution, the probability density distribution law can be expressed as in Eq. (2).

$$\ln(-\ln\frac{\sigma}{E\varepsilon}) = m\ln F - m\ln F_0. \tag{2}$$

Let y = ln (-ln ($\sigma/E\varepsilon$)); x = ln F; b = -$m$ln F_0. Parameters m and F_0 were obtained by fitting the test data under uniaxial compression.

Statistical Constitutive Models of Rock Macro-damage

Based on the defined additional strain energy of rock macro-damage by Chen and Li (2000), the damage strain energy can be expressed using Eq. (3).

$$D_2 = \begin{cases} 0, \tan\alpha < \tan\varphi \\ 1 - \dfrac{1}{1 + \dfrac{2}{V\sigma^2}\left(\int_0^A (K_{\mathrm{I}}^2 + K_{\mathrm{II}}^2)dA + 2\int_0^l (K_{\mathrm{I}}^2 + K_{\mathrm{II}}^2)dl\right) + \dfrac{4Ea(f\sigma_n)\delta}{V\sigma^2}}, \tan\alpha \geq \tan\varphi \end{cases} \tag{3}$$

where α denotes the joint inclination angle, a denotes the half-length joint, φ denotes the internal friction angle of the rock material ($f = \tan\varphi$), V denotes the volume of the elastomer, σ_{n} denotes the normal stress on the joint surface and δ denotes the amount of relative slip caused by the joint surface area A, crack expansion length l and shear stress. Three parameters can be calculated with relative expressions from previous studies (Chen and Li, 2000; Grady and Kipp, 1980; Nemat and Obata, 1988). The stress-intensity factor of a single joint is different from that of multi-row parallel discontinuous joints, as expressed in Eq. (4) (Huang et al., 2002; Li et al., 2001).

$$\left.\begin{aligned} K_{\mathrm{I}} &= \left(-\frac{2a\tau_{eff}\sin\theta}{\sqrt{\pi(l+l_*)}} + \sigma_{\mathrm{n}}(\sigma,\alpha+\theta)\sqrt{\pi l}\right)\sqrt{\sec\left(\frac{\pi a}{w}\right)} \\ K_{\mathrm{II}} &= \left(-\frac{2a\tau_{eff}\cos\theta}{\sqrt{\pi(l+l_*)}} - \tau_{\mathrm{n}}(\sigma,\alpha+\theta)\sqrt{\pi l}\right)\sqrt{\sec\left(\frac{\pi a}{w}\right)} \end{aligned}\right\} , \tag{4}$$

where K_{I} and K_{II} are the multi-joint type-I and type-II stress-intensity factors, respectively. $l_* = 0.27a$ and w is the width of the specimen. The sliding shear strength of the joint surface τ_{eff}, normal stress $\sigma_{\mathrm{n}}(\sigma, \alpha + \theta)$ and shear stress $\tau_{\mathrm{n}}(\sigma, \alpha + \theta)$ can be calculated using the expression given by Li et al. (2001). The stress-intensity factor of multi-row parallel intermittent joints must consider the coupling effect of the joints, as shown in Eq. (5).

$$\left.\begin{aligned} K_{\mathrm{I}} &= f(a,b,d)K_{\mathrm{I0}} \\ K_{\mathrm{II}} &= f(a,b,d)K_{\mathrm{II0}} \end{aligned}\right\} , \tag{5}$$

where K_{I0} and K_{II0} are single-joint type-I and type-II stress-intensity factors, respectively and $f(a, b, d)$ is the interaction coefficient. Moreover, b denotes the joint centre distance and d denotes the joint arrangement distance. This is because two rows of two parallel intermittent joints are considered in this study. The coefficients are supplemented by interpolation in Table 1 and the raw data is derived from the study by Li et al. (2001). Three values; namely, $(d/2a, b/2a) = (0,0)$, $(0.5, 0)$ and $(0.6, 0)$, were considered to couple the damage variables according to the experimental data in Table 2.

Table 1. Values of *f* (*a, b, d*) (Li *et al.*, 2001)

d*/2*a	***b*/2*a***						
	∞	**5**	**2.5**	**1.67**	**1.25**	**0.5**	**0**
∞	1.000	1.017	1.075	1.208	1.565	2.203	2.628
5	1.016	1.020	1.075	1.208	1.565	2.203	2.628
1	1.257	1.257	1.258	1.292	1.580	2.094	2.437
0.6	1.703	1.703	1.704	1.720	1.861	2.112	2.280
0.5	1.815	1.815	1.815	1.827	1.931	2.117	2.241
0.25	2.094	2.094	2.094	2.094	2.107	2.130	2.145
0	2.373	2.373	2.373	2.361	2.283	2.144	2.051

Table 2. Physical and geometric joint parameters

Joint types	E_0/ GPa	φ/(°)	Joint arrangement distance d/mm	Joint center distance b/mm	Joint length $2a$/mm	Joint depth B/mm	Joint numbers per unit area ρ/mm^2
Complete	12.474	25	0	0	0	150	0
Single	9.922		0		60	150	4.444×10^{-5}
Double	6.130		30		60	150	8.889×10^{-5}
Three	8.404		30		50	150	1.333×10^{-4}

When there are single-group multi-row joints in rock masses, the macro-damage variable D_2 can be obtained by substituting Eq. (5) into Eq. (3) to obtain Eq. (6).

$$D_2=\begin{cases} 0,\ \tan\alpha<\tan\varphi \\ 1-\{1+\dfrac{2}{V}[4.72NBa^2\cos^2\alpha(\sin\alpha-\cos\alpha\tan\varphi)^2+\dfrac{8NBa^2\cos^2\alpha(\sin\alpha-\cos\alpha\tan\varphi)^2}{\pi} \\ \ln(l+\dfrac{l}{l_*})+\dfrac{\pi}{2}(1+\cos 2(\alpha+\theta)l^2+8\sqrt{2}NBa^2\cos\alpha(\sin\alpha-\cos\alpha\tan\varphi)\tan\varphi \qquad ,\tan\alpha\geq\tan\varphi \\ \sqrt{\dfrac{l+l_{**}}{l+l_*}}]f^2(a,b,d)\sec(\dfrac{\pi a}{w})\}^{-1} \end{cases} \tag{6}$$

Macro-meso Coupling Damage Constitutive Model

For the coupling calculation problem between two scale damage variables, the expression of the rock coupling-damage variable was obtained from two studies (Liu et al., 2016a; Zhang et al., 2015).

$$D_{12}=1-\frac{(1-D_1)(1-D_2)}{1-D_1D_2} \tag{7}$$

where D_{12} is the coupling-damage variable, D_1 is the meso-scopic damage variable and D_2 is the macro-damage variable. The coupling-damage constitutive model of intermittent rock masses can be obtained by substituting D_{12} into Eq. (1).

$$\sigma=E_0\varepsilon(1-D_{12})=E_0\varepsilon\frac{(1-D_1)(1-D_2)}{1-D_1D_2} \tag{8}$$

Cases Analysis and Model Verification

Impact of Statistical Parameters on the Model

The macro-meso coupling-damage constitutive model of intermittent joint rock masses has been applied to fractured rock masses (Chen and Qiao, 2018b). For the damage analysis of rock-like masses using the model derived by Figure 1, the experimental data was obtained from two sources (Sun et al., 2018; Sun et al., 2019). In this study, the joint inclination angle and number of joints were regarded as variables to investigate the strength and deformation characteristics of plain concrete. Stainless-steel sheets with a thickness of 0.3 mm and a length of 160 mm were pre-fabricated with four types of joint specimens. These are complete, single-joint, double-joint and triple-joint specimens (Figure 2). All joints were through and the main joint inclination angles α were 0°, 30°, 45°, 60° and 90°. Model tests were conducted under uniaxial compression. The dimensions of the specimens were 150 mm × 150 mm × 150 mm. The physical and geometric parameters of the joint specimens are presented in Table 2.

In Table 2, the elastic modulus is the average value obtained by fitting the stress-strain data in the uniaxial compression tests. The ability of the complete specimens to resist the elastic deformation was significantly larger than that of the joint specimens. There were some differences in the different joint types of the specimens. By substituting the rock mechanical parameters of the complete specimens (Sun et al., 2019) into the statistical damage constitutive model, the statistical parameters m = 0.833 and F_0 = 9.573 MPa were obtained using the fitting method. Figure 3 shows the effect curve in which the constitutive model of plain concrete is affected by these two parameters.

Figure 3a shows the effect of F_0 on the constitutive model of plain-concrete specimens when m = 0.833. The stress in the linear elastic stage is hardly affected by the change in F_0. However, the stress in the non-linear elastic stage gradually decreases with an increase in F_0 and the curve shows parallel characteristics when the strength reaches its peak value. This indicates that F_0 reflects the average value of the micro-element strength of plain concrete (Yang et al., 2004). Figure 3b shows the effect of m on the constitutive model for F_0 = 9.573 MPa. The stress in the linear elastic stage changes slightly with an increase in m. The stress in the non-linear elastic stage has a positive correlation with m when the strength reaches the peak value. When the strain is 0.101%, the curvature of the post-peak curve becomes steeper with an increase in m. Notably, m is a measure of the ductility and brittleness of the material. Parameter m reflects the degree of concentration of the micro-element strength distribution in plain concrete (Yang et al., 2004).

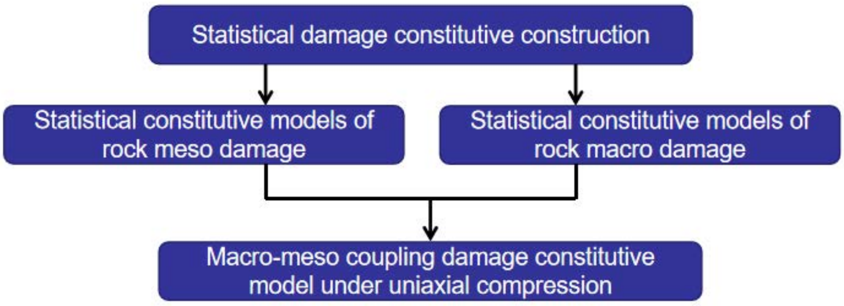

Figure (1): Schematic representation of the methodology

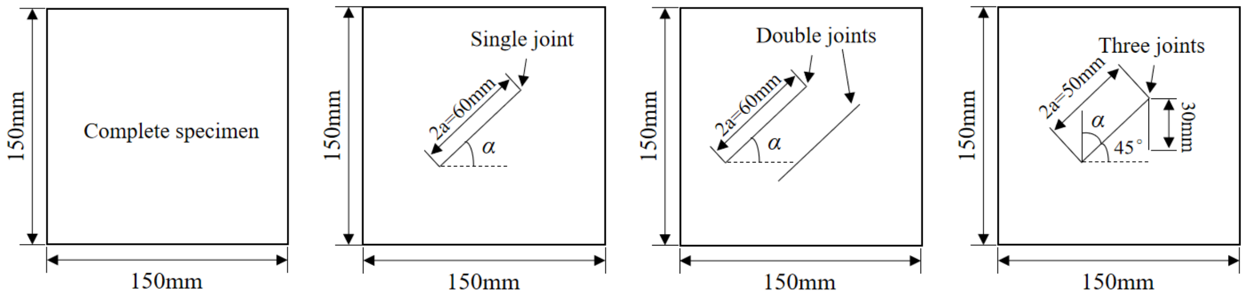

a) b) c) d)

Figure (2): Sketch map of plain concrete specimens with different formal joints: a) complete b) single joint c) double joints and d) three joints

Calculation of Damage Variables for Plain Concrete

Under uniaxial compression, the crack-growth length l along the principal stress after the plain concrete is damaged is shown in Table 3. The crack length indicates the degree of macro-scopic damage from a one-dimensional perspective. Because the loading process is continuous, it is difficult to accurately quantify the relationship between crack-growth length and strain change. The total crack-growth length was evenly distributed in each loading step. This can be used as the basis for calculating D_2. The damage variables can exhibit failure characteristics to a certain extent. Figure 4 shows the micro-scopic damage variable graphs and macro-microscopic coupling-damage variable graphs for different joint types during specimen failure.

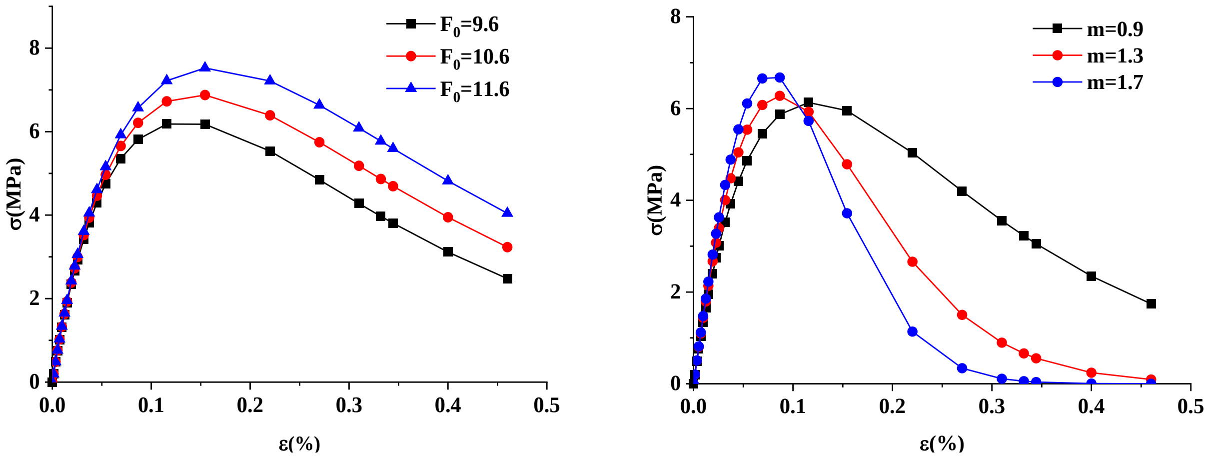

a) b)

Figure (3): Statistical parameters' effects on constitutive models: a) F_0 value and b) m value

Table 3. Crack length

Joint type **Joint angle**	**Single-joint specimens**	**Double-joint specimens**	**Three-joint specimens**
0°	75.000	60.000	57.300
30°	60.000	40.500	56.600
45°	53.800	43.200	57.300
60°	49.000	44.500	49.600
90°	45.000	45.000	36.100

Figure 4a shows the curves of D_1 and ε for a single joint. Figure 4b shows the curves of D_{12} and ε for a single joint. Comparing Figure 4a and Figure 4 b, the coupling damage of a single joint was dominated by meso-scopic damage. The damage evolution rate of 45° joint specimens was the fastest when the damage value was less than 0.80 and the rate gradually weakened when the damage value was more than 0.80. These results were consistent with those obtained by Sun et al. (2018). Additionally, the damage evolution rates for other joint inclination angles are respectively complete; 90°, 0°, 60° and 30° joint specimens go from fast to slow in a loading process. These results are consistent with conclusions obtained by Chen et al. (2018a). Meanwhile, it was indicated that the existence of joints weakens the strength and elastic modulus, which results in a brittle to ductile failure transition. The damage rates of all specimens tended to stabilize when the damage variable was equal to 0.80. Once the specimens were close to damage, the damage value was the largest for the complete specimen. This indicates that the ability of the complete specimen to resist the development of micro-cracks and voids is stronger than those of the joint specimens.

Figure 4c shows the curves of D_1 and ε double joints. Figure 4d shows the curves between D_{12} and ε for double joints. In Figure 4c, the meso-scopic damage evolution rates of 45° and 60° specimens were smaller than those of other joint specimens. In Figure 4d, 45° and 60° specimens' coupling damage rates are significantly larger than those of other joint specimens before D_{12} was 0.80. The rate became smaller than those of other specimens after D_{12} reached 0.80. This indicates that the damage evolution rate is closely correlated with the macro-scopic joint numbers of the double-joint specimens under uniaxial compression. The coupling-damage evolution rates for other joint inclination angles are complete; 0°, 90° and 30° specimens, from fast to slow. The damage rates of all the specimens tended to be stable when the specimens were almost damaged. This indicates that micro-cracks and voids have a critical threshold and this value is related only to the material characteristics and macro-scopic joint damage.

Figure 4e shows the curves of D_1 and ε for the triple-joint specimens. Figure 4f shows the curves between D_{12} and ε for the triple-joint specimens. Comparing Figure 4e and Figure 4 f, the damage evolution rates of the 30°, 45° and 60° joint specimens are the largest when the damage value is less than 0.25. The damage accumulation of the 45° and 60° joint specimens was the largest when this value was between 0.25 and 0.50. The damage rate of the 30° joint specimen was the smallest and other joint specimens were basically similar during the loading process. The greater the damage evolution rate, the earlier the damage to the specimens. This is consistent with the experimental results, in which 45° and 60° joint specimens exhibited brittle failure and 30° joint specimen exhibited ductile failure (Sun et al., 2019).

Figure 5 shows curves of different numbers of joints between D_{12} and ε at different joint inclination angles, including 0°, 30°, 45°, 60° and 90°. In Figure 5a, when D_{12} is below 0.80, the damage evolution rates for the 0° joint specimens are: triple-joint, complete joint, single-joint and double-joint specimens from large to small, respectively. The reason for the fastest damage of the triple-joint specimens has a close correlation to the connectivity between primary and secondary joints. When D_{12} is more than 0.80, it tends to remain constant. Moreover, the damage value of the complete specimens is more than that of the joint specimens. In Figure 5b, when D_{12} is below 0.25, the damage rate of the 30° double-joint and triple-joint specimens is the largest, while that of the single-joint specimens is the smallest. When D_{12} is more than 0.25, the damage rate of complete specimens is faster than that of joint specimens and the damage value is the largest. In Figure 5c and Figure 5d, when D_{12} is below 0.50, the damage accumulation of double-joint and triple-joint specimens (45°, 60°) is the largest. When D_{12} is between 0.50 and 0.80, the damage rate of the 45° single-joint specimens is the largest and that of the 60° single-joint specimens is the smallest. When D_{12} is more than 0.80, the damage rate of the 45° and 60° specimens is approximately similar to those of the triple-joint and complete specimens. However, the damage value of the complete specimens is 0.972 and is more than those of other joint specimens. In Figure 5e, the coupling damage value of the 90° joint specimens is approximately similar to that of the 0° specimens.

Comparing Figures 4 and 5, for the single-joint specimens, the damage rate of the 45° joint specimens was the fastest at the initial stage of loading. However, for the 30°-joint specimens the damage rates the slowest. When D_{12} reached 0.80, the damage rate of the joint specimens gradually decreased and it was lower than that of the complete specimens. For the double-joint specimens, the damage rates of the 45° and 60° joint specimens were the highest at the initial stage of loading. This rate decreased until D_{12} reached 0.50. Moreover, the turning point of the damage evolution of the 30° joint specimens is equal to 0.25. The damage rate, including that of the 0° and 90° joint specimens, was the smallest during the entire loading process. For the triple-joint specimens, the turning point of the damage evolution of the 0° joint specimens is equal to 0.80. Certain specimens, including 30°, 45° and 60° joints, have damage evolution characteristics that are similar to those of the double-joint specimens. The damage rate of the 90° joint specimens was greater than that of other joint specimens in the initial stage of loading. The early evolution of specimens is increasingly faster for single-joint, double-joint and triple-joint specimens. This result had a positive correlation with the degree of structural damage as the number of joints increased. During the uniaxial loading process, the damage curves obeyed the *S*-type evolution law: they first increased and then decreased. This is consistent with the experimental results.

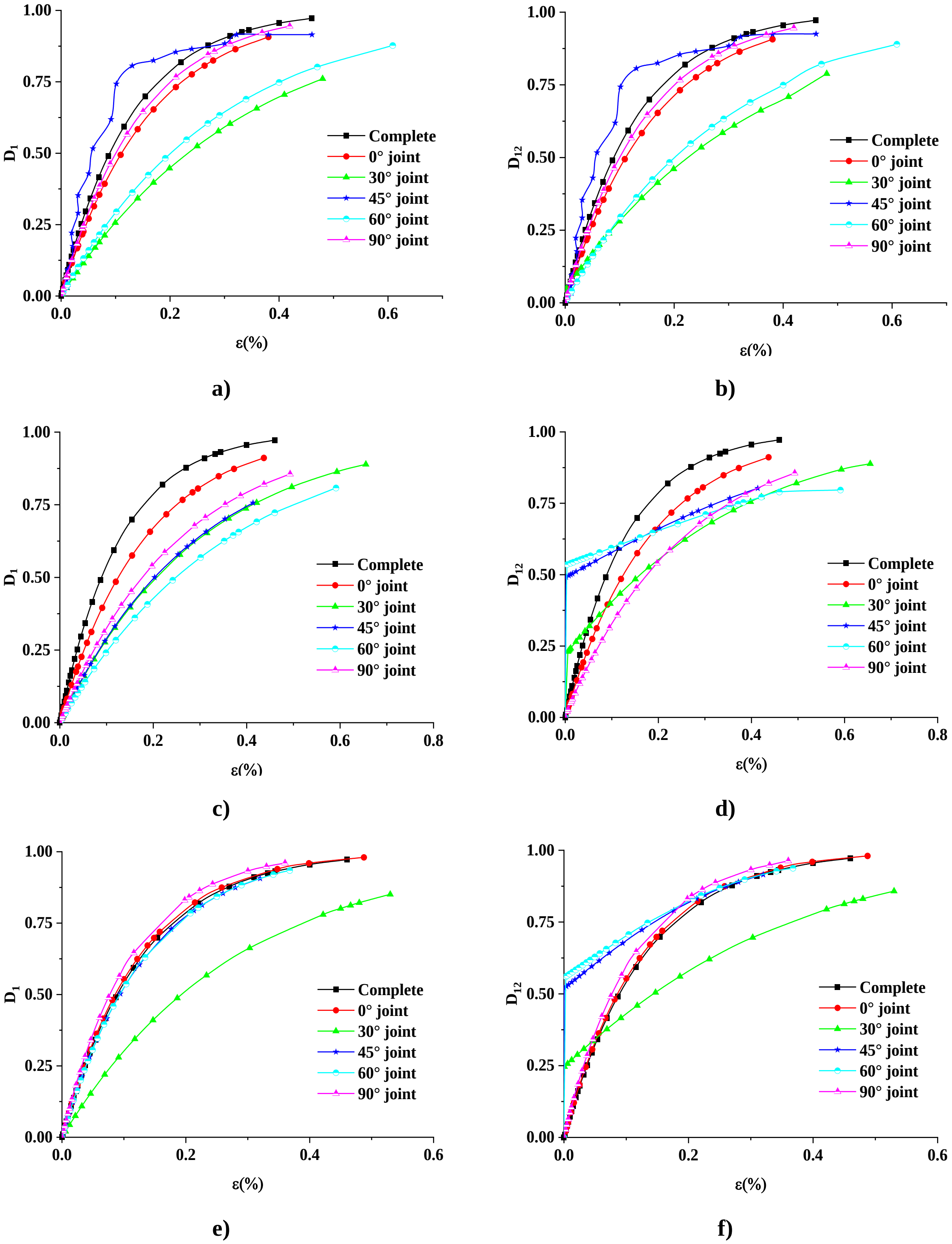

a) b) c) d) e) f)

Figure (4): Curves of the damage variable and strain for different joint numbers: a) ε-D_1 of single joint b) ε-D_{12} of single joint c) ε-D_1 of double joints d) ε-D_{12} of double joints e) ε-D_1 of three joints and f) ε-D_{12} of three joints

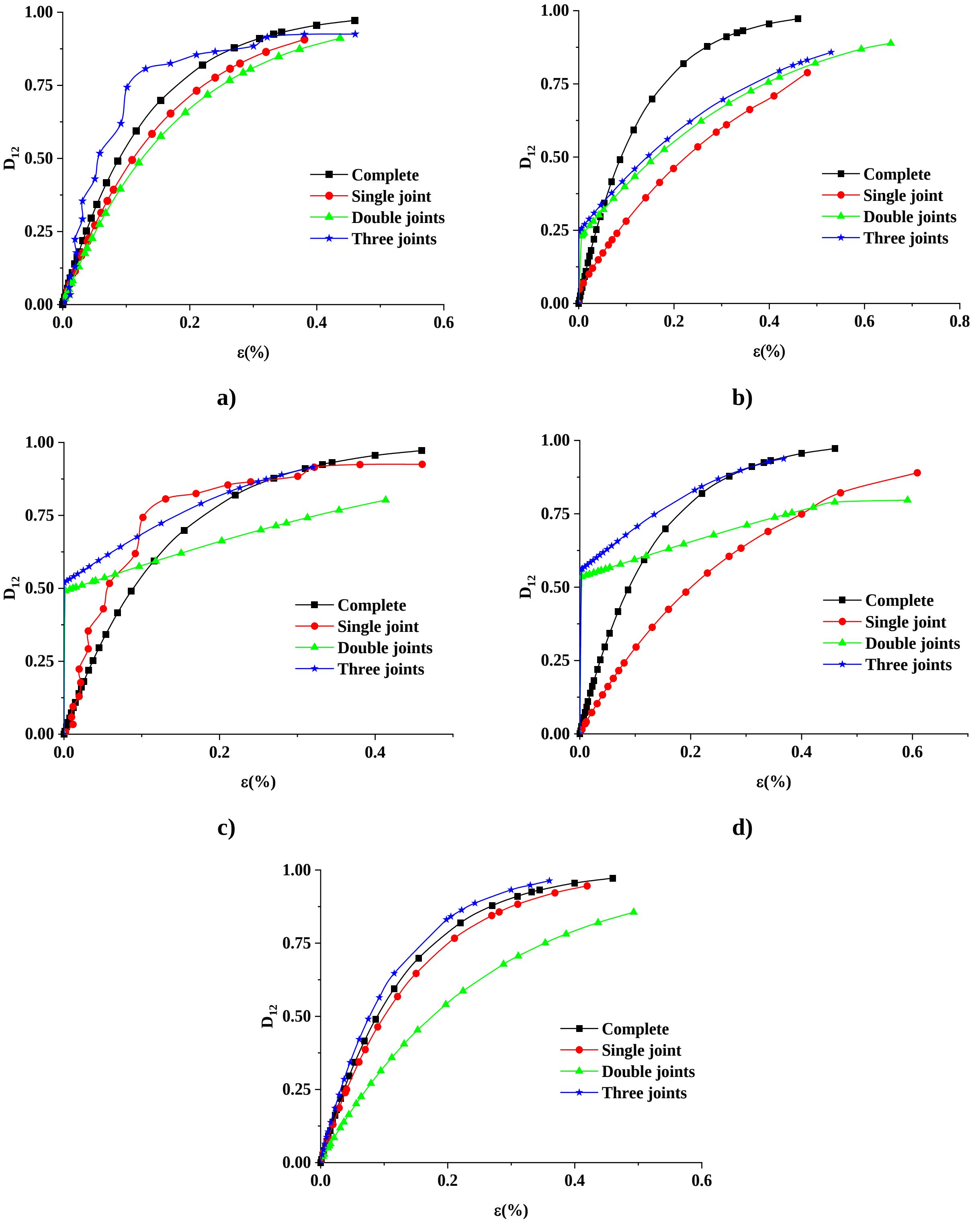

a) **b)** **c)** **d)** **e)**

Figure (5): Curves between the macro-meso-coupling damage variable and strain in different joint angles: a) 0° b) 30° c) 45° d) 60° and e) 90°

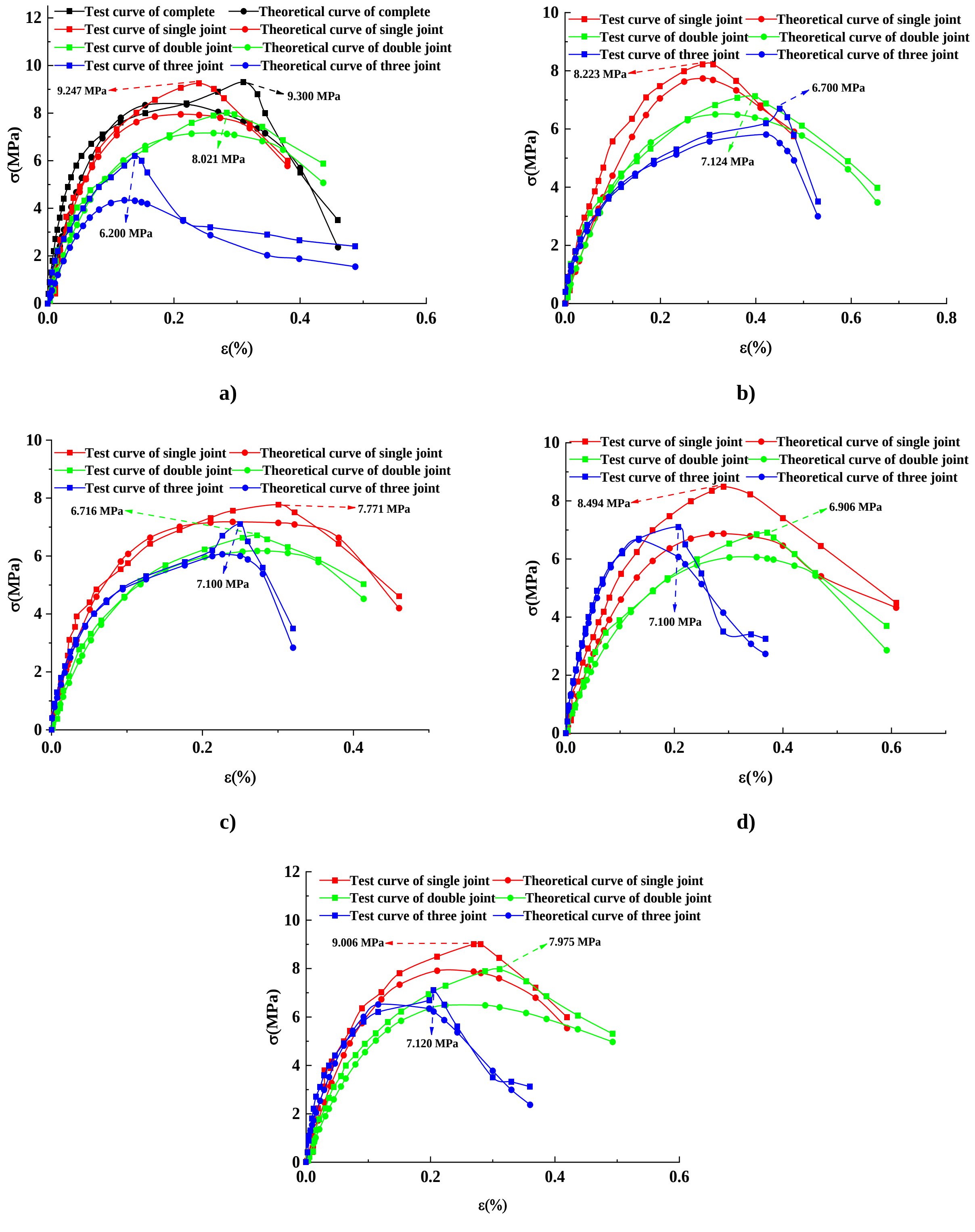

a)

b)

c)

d)

e)

Figure (6): Experimental and theoretical curves under different joint numbers and inclination angles: a) 0° b) 30° c) 45° d) 60° and e) 90°

Comparison between Theoretical and Experimental Constitutive Curves

Theoretical constitutive curves of complete, single-, double- and triple-joint specimens can be obtained by substituting the macro-meso coupling damage variables into Eq. (8). Subsequently, they are compared with experimental constitutive curves from two sources (Chen et al., 2011), as shown in Figure 6.

In Figure 6, the theoretical and experimental constitutive curves for each set of joint types match well at the linear elastic stage, indicating that the damage degree of plain concrete is small at the beginning of loading. However, a slight difference is observed at the plastic stage. This difference may be related to the crack length deviation, because the crack path is a curve instead of a straight line.

In Figure 6a, the elasticity modulus and peak strength of the complete specimens are larger than those of the joint specimens, which shows that the ability of plain concrete to resist deformation is weakened by cracks. The peak strengths of the specimens are arranged in increasing values such that single-joint > double-joint > triple-joint specimens. The test and theoretical peak strengths are 9.247, 8.021 and 6.200 and 7.948, 7.159 and 4.340 MPa, respectively. The reductions in the peak strength were up to 14%, 11% and 30%. In Figure 6b, the peak strength follows the same rule as the 0° joint specimens. The test and theoretical peak strengths are 8.223, 7.124 and 6.700 and 7.736, 6.501 and 5.808 MPa, respectively. The reductions in the peak strength were up to 6%, 9% and 13%. In Figure 6c, the peak strength of the single-joint specimens is the largest, but that of the double-joint specimens is lower than that of the triple-joint specimens. The test and theoretical peak strengths are 7.771, 6.716 and 7.100 MPa and 7.179, 6.174 and 6.060 MPa, respectively. The reductions in the peak strength were up to 8%, 8% and 15%. In Figure 6d, the peak strength followed the same rule as the 45° joint specimens. The test and theoretical peak strengths are 8.494, 6.906 and 7.100 and 6.873, 6.062 and 6.661 MPa, respectively. The reductions in the peak strength were 19%, 12% and 6%. In Figure 6e, the peak strength followed the same rule as the 0° joint specimens. The test and theoretical peak strengths are 9.006, 7.975 and 7.120 MPa and 7.909, 6.484 and 6.519 MPa, respectively. The reductions in the peak strength were up to 12%, 19% and 8%. The maximum peak strength (9.300 MPa) occurred in the complete specimens. However, the minimum peak strength occurred in the 0° triple-joint specimens and its value was 6.200 MPa. The reduction in the peak strength was up to 33% owing to the presence of joints.

It is evident that the peak strengths of the 0°, 30° and 90° joint specimens are single-joint, double-joint, triple-joint specimens from large to small, respectively. However, for the 45° and 60° joint specimens, the peak strength of the double-joint specimens was lower than that of the triple-joint specimens. This is because the double-joint specimens were prone to rock mass failure along the 45° direction under multi-crack distribution and the above results correspond to curves of damage variables in Figure 5c and Figure 5d. A comparative analysis of the theoretical and experimental constitutive curves revealed that the improved damage constitutive models can be applied to plain concrete.

Fractal Characteristics of a Fractured Surface in Rock-like Specimens

Basic Principles of Fractal-box Dimensions

The failure mechanism can be characterized by the macroscopic fracture-surface morphology. The fracture morphology is calculated using the fractal-box dimensions calculated in plain concrete (Zou et al., 2016). The variable is defined as follows: Let A be any non-empty and bounded sub-set of the R_n space. When $r > 0$, A is covered by n-dimensional cubes of side length r. The minimum coverage is $N_r(A)$. If d is present, r tends to zero.

$$N_r(A) \propto \frac{1}{r^d} \quad , \tag{9}$$

where d denotes the box dimensions of A. Only a positive number k exists and Eq. (10) can be established as follows:

$$\lim_{r\to 0}\frac{N_r(A)}{1/r^d}=k \, . \tag{10}$$

Fractal dimension d can be obtained by taking the logarithm on both sides of Eq. (10).

$$d=\lim_{r\to 0}\frac{\lg k-\lg N_r(A)}{\lg r}=-\lim_{r\to 0}\frac{\lg N_r(A)}{\lg r}. \tag{11}$$

$N_r(A)$ is calculated at different values of r to cover A. Let lg r be the horizontal axis and lg $N_r(A)$ be the vertical axis. (lg r_i, lg $N_{ri}(A)$) can be drawn in the coordinate system. All coordinate scatters were fitted using MATLAB and the absolute value of the straight-line slope represented the fractal box dimensions.

Fractal Dimension Calculation of a Fracture Surface in Plain Concrete Specimens

In the above analysis of the constitutive models, the effect of cracks on the fracture process of plain concrete was revealed by introducing the crack length to calculate the macro-scopic damage variable. Similarly, the fractal-box dimensions of the joint surface can be used as a quantitative indicator of the macro-scopic damage variable.

In Figure 7, the fractal-box dimensions of the complete specimens amounted to 1.737. In single-joint specimens, the fractal-box dimensions (45°) were the largest, at a value of 1.772 and the fractal-box dimensions (30°) were the smallest, at a value of 1.617. Among the double-joint specimens, the fractal-box dimensions (60°) were the largest, at a value of 1.785. For 90° and joint specimens, the fractal-box dimensions were the smallest, at a value of 1.670. Among triple-joint specimens, the fractal-box dimensions (60°) were the largest, at a value of 1.778. The 30° joint specimens showed the smallest value at 1.736.

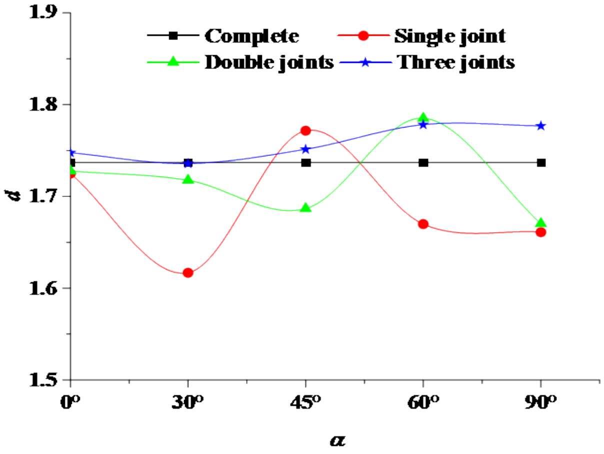

Figure (7): Curves of the joint inclination angle and fractal-box dimensions under different joint numbers

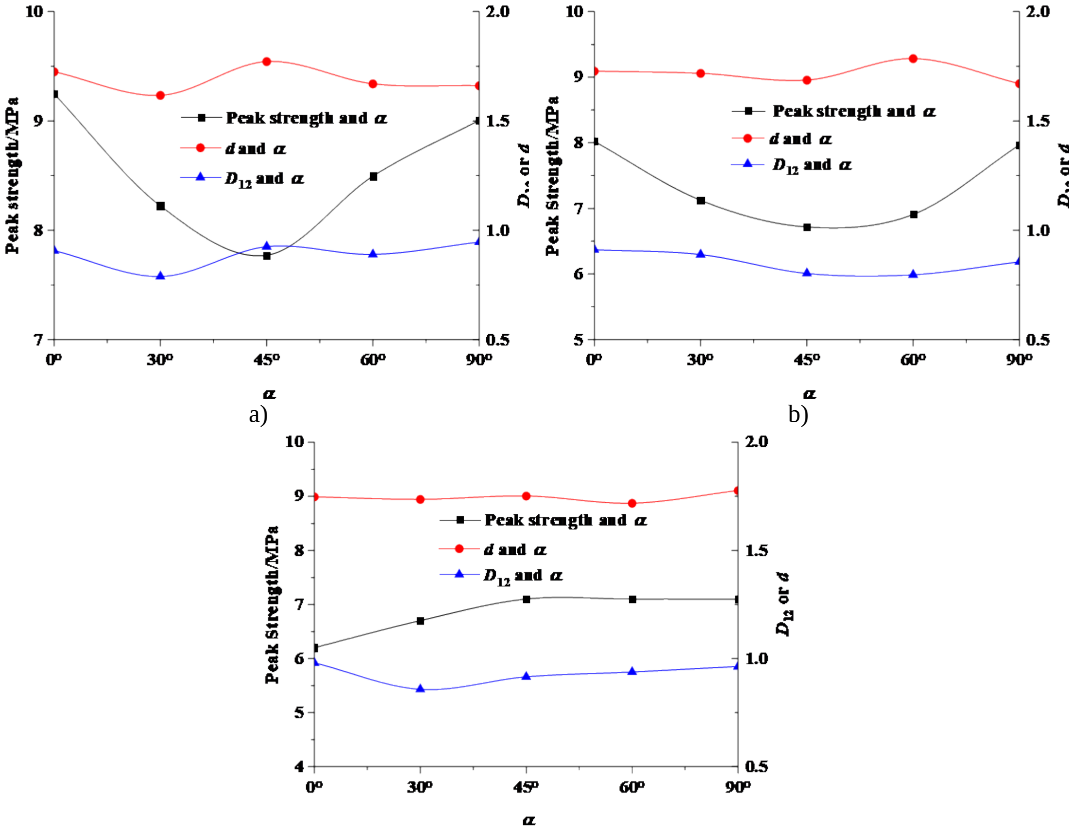

a)

b)

Figure (8): Curves of the peak strength, box dimensions, coupling damage variable and joint inclination angle: a) single joint b) double joints and c) three joints

These results are consistent with the damage variables shown in Figures 4 and 5. The fractal-box dimensions can be used as a measure of the macroscopic damage in rock-like masses. In Figure 8a, a smaller experimental peak strength resulted in larger fractal-box dimensions and a larger coupling-damage value. This indicates that the ability of plain concrete to resist plastic deformation was weak. As shown in Figures 8b and 8c, the joint inclination angle has similar characteristics to these variables, including peak strength, coupling damage value and fractal-box dimensions.

CONCLUSIONS

- The macro-meso coupling damage constitutive model introduced from the damage analysis of intermittent fractured rock masses can be applied to plain concrete. The damage rate of joint concrete increases with an increase in the number of joints at the initial stage of loading. The damage curves obey the *S*-type evolution law during the entire uniaxial compression process.
- The joint inclination angle and the number of joints are important factors that contribute to the damaging of concrete materials. Different joint inclination angles lead to different damage rates, where single- (45°), double- (45°, 60°) and triple-joint (0°, 90°) specimens have the fastest damage rates.
- The elastic modulus and the peak strength of the single-joint specimens are close to those of the complete specimens. Most double-joint specimens have values less than those of complete specimens. All the triple-joint specimens have values that are further less than those of complete specimens. The inherent damage to plain concrete increases as the number of joints increases.
- The peak strength, coupling damage value and fractal-box dimensions can reflect the fracture conditions of the jointed concrete. A smaller peak strength results in larger fractal box dimensions and a larger coupling-damage value.

Acknowledgments

This work was financially supported by the National Natural Science Foundation of China (Grant no. 51708466).

REFERENCES

Bobet, A., and Einstein, H.H. (1998). “Fracture coalescence in rock-type materials under uniaxial and biaxial compression.” International Journal of Rock Mechanics and Mining Sciences, 35 (7), 863-888.

Cao, W.G., Zhao, C., He, M., and Liu T. (2017). “Voids’ change and statistical damage simulation method of the full deformation process for rocks.” Journal of Hunan University (Natural Sciences), 44 (9), 100-106.

Chen, X., Liao, Z.H., and Li, D.J. (2011). “Experimental study of effects of joint inclination angle and connectivity rate on strength and deformation properties of rock masses under uniaxial compression.” Chinese Journal of Rock Mechanics and Engineering, 30 (4), 781-789.

Chen, S., Qiao, C.S., Ye, Q., and Deng B. (2018a). “Composite damage constitutive model of rock mass with intermittent joints based on Mohr-Coulomb criterion.” Rock and Soil Mechanics, 39 (10), 3612-3622.

Chen, S., and Qiao, C.S. (2018b). “Composite damage constitutive model of jointed rock mass considering crack propagation length and joint friction effect.” Arabian Journal of Geo-sciences, 11 (11), 1-11.

Chen, W.L., and Li, N. (2000). “Damage model of the rock mass medium with intermittent cracks.” Chinese Journal of Geo-technical Engineering, 22 (4), 430-434.

Fan, X., Chen, R., Lin, H., Lai, H.P., Zhang, C.Y., and Zhao, Q.H. (2018). “Cracking and failure in rock specimens containing combined flaw and hole under uniaxial compression.” Adv Civ. Eng., (5), 1-15.

Grady, D.E., and Kipp, M.E. (1980). “Continuum modeling of explosive fracture in oil shale.” International Journal of Rock Mechanics and Mining Sciences, 17 (3), 147-157.

Guan, X., and Chen J. X. (2021). “Statistical damage constitutive model of shotcrete under axial compression.” Jordan Journal of Civil Engineering, 15 (3), 445-460.

Hoek, E., and Bieniawski, Z.T. (1965). “Brittle fracture propagation in rock under compression.” International Journal of Fracture, 1 (3), 137-155.

Huang, C.Y., Subhash, G., and Vitton, S.J. (2002). “A dynamic damage growth model for uniaxial compressive response of rock aggregates.” Mechanics of Materials, 34 (5), 267-277.

Kawamoto, T., Ichikawa, Y., and Kyoya, T. (1988). “Deformation and fracturing behavior of discontinuous rock mass and damage mechanics theory.” International Journal for Numerical and Analytical Methods in Geo-mechanics, 12 (1), 1-30.

Lemaitre, J. (1984). “How to use damage mechanics.” Nuclear Engineering and Design, 80 (2), 233-245.

Li, N., Chen, W., Zhang, P., and Swoboda, G. (2001). “The mechanical properties and a fatigue-damage model for jointed rock masses subjected to dynamic cyclical loading.” International Journal of Rock Mechanics and Mining Sciences, 38 (7), 1071-1079.

Lin, Q., Cao, P., Meng, J., Cao, R., & Zhao, Z. (2020). “Strength and failure characteristics of jointed rock mass with double circular holes under uniaxial compression: Insights into discrete-element method modeling”. Theoretical and Applied Fracture Mechanics, 109, 102692.

Liu, H.Y., Yang, Y., Li, J.F., and Zhang, L.M. (2016). “Dynamic damage constitutive model for rock mass with non-persistent joints based on the TCK model.” Explosion and Shock Waves, 36 (3), 319-325.

Liu, H.Y., Wang, X.S., Zhang, L.M., and Zhang, L.G. (2016). “A dynamic damage constitutive model for rock mass with non-persistent joints under uniaxial compression.” Chinese Journal of Geo-technical Engineering, 38 (3), 426-436.

Nemat, N.S., and Obata, N.A. (1988). “A micro-crack model of dilatancy in brittle materials.” Journal of Applied Mechanics, 55 (1), 24-35.

Qing, W.R., Qiang, L., and Ya, J.Y. (2018). “Concrete meso-structure characteristics and mechanical-property research with numerical methods.” Construction and Building Materials, 158, 189-197.

Sun, B., Zou, C.H., Zeng, S., Fang, Y.C., and Wang, F.L. (2018). “Failure characteristics of rock-like mass with different fracture types under uniaxial compression.” Journal of Disaster Prevention and Mitigation Engineering, 38(6), 959-966.

Sun, B., Luo, Y., Xie, J.H., and Zeng, S. (2019). “Failure test of *N*-type combination jointed rock mass under uniaxial compression.” Gold Science and Technology, 27 (4), 548-556.

Thomas, P.F.T., and Belytschko, T. (2010). “The extended generalized finite-element method: An overview of the method and its applications.” International Journal for Numerical Methods in Engineering, 84(3), 253-304.

Yang, D.F., Zhang, D.Y., Niu, S.J., Ge, S.J., Liu, S., Chen, X., Wang, T.T., and Li, X.Y. (2019). “Experimental study on crack-propagation process and macro-scopic failure mode of pre-fabricated-crack fine sandstone under uniaxial compression.” Journal of Mining & Safety Engineering, 36 (4), 786-793.

Yang, S.Q., Xu, W.Y., Wei, L.D., and Su, C.D. (2004). “Rock damage constitutive model and experimental study under uniaxial compression.” Journal of Hohai University (Natural Sciences), 32 (2), 200-203.

Yousuf, S., Shafigh, P., Ibrahim, Z., Hashim, H., and Panjehpour, M. (2019). “Cross-over effect in cement-based materials: A review.” Applied Sciences, 9 (3), 1-18.

Zeng, S., Jiang, B., and Sun, B. (2019). “Experimental study on the mechanical properties and crack propagation of jointed rock mass under impact load.” Geotech. Geol. Eng., 37, 5359-5370.

Zhang, P., and Chen, C. (2017). “Constitutive model of rock mass damage considering the mechanical properties of intermittent joints.” Highways & Automotive Applications, (4), 180-184.

Zhang, L.M., Lv, S.R., and Liu, H.Y. (2015). “A dynamic damage constitutive model of rock mass by comprehensively considering macro-scopic and meso-scopic flaws.” Explosion and Shock Waves, 35 (3), 428-436.

Zhou, W.Y., Yan, G.R., and Yang, R.Q. (1998). “Elastic-brittle damage model for rock mass based on field tests in Laxiwa arch dam site.” Chinese Journal of Geo-technical Engineering, 20 (5), 54-57.

Zou, J.P., Chen, W.Z., Yang, D.S., Yu, H.D., and Tan, X.J. (2016). “Micro-structural characteristics of low-rank coal from Hunchun based on SEM.” Chinese Journal of Rock Mechanics and Engineering, 35 (9), 1805-1814.